Heliyon 10 (2024) e23013

Contents lists available at ScienceDirect

Heliyon

journal homepage: www.cell.com/heliyon

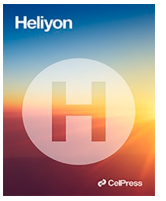

Quantitative multi-energy micro-CT: A simulation and phantom study for simultaneous imaging of four different contrast materials using an energy integrating detector

Andrea Kronfeld [a,*], Patrick Rose [a,b], Jan Baumgart [c], Carolin Brockmann [a], Ahmed E. Othman [a], Bernd Schweizer [b], Marc Alexander Brockmann [a]

[a] University Medical Center of the Johannes Gutenberg University Mainz, Department of Neuroradiology, Langenbeck 1, 55131, Mainz, Germany
[b] RheinMain University of Applied Sciences, Faculty of Engineering, Am Brückweg 26, 65428, Rüsselsheim am Main, Germany
[c] University Medical Center of the Johannes Gutenberg University Mainz, Translational Animal Research Center, Hanns-Dieter-Hüsch-Weg 19, 55128, Mainz, Germany

ARTICLE INFO

Keywords:
Multi-energy CT
Micro-CT
Simulation
Phantom
Matrix inversion

ABSTRACT

Emerging from the development of single-energy Computed Tomography (CT) and Dual-Energy Computed Tomography, Multi-Energy Computed Tomography (MECT) is a promising tool allowing advanced material and tissue decomposition and thereby enabling the use of multiple contrast materials in preclinical research.

The scope of this work was to evaluate whether a usual preclinical micro-CT system is applicable for the decomposition of different materials using MECT together with a matrix-inversion method and how different changes of the measurement-environment affect the results.

A matrix-inversion based algorithm to differentiate up to five materials (iodine, iron, barium, gadolinium, residual material) by applying four different acceleration voltages/energy levels was established. We carried out simulations using different ratios and concentrations (given in fractions of volume units, VU) of the four different materials (plus residual material) at different noise-levels for 30 keV, 40 keV, 50 keV, 60 keV, 80 keV and 100 keV (monochromatic). Our simulation results were then confirmed by using region of interest-based measurements in a phantom-study at corresponding acceleration voltages. Therefore, different mixtures of contrast materials were scanned using a micro-CT. Voxel wise evaluation of the phantom imaging data was conducted to confirm its usability for future imaging applications and to estimate the influence of varying noise-levels, scattering, artifacts and concentrations.

The analysis of our simulations showed the smallest deviation of 0.01 (0.003–0.15) VU between given and calculated concentrations of the different contrast materials when using an energy-combination of 30 keV, 40 keV, 50 keV and 100 keV for MECT. Subsequent MECT phantom measurements, however, revealed a combination of acceleration voltages of 30 kV, 40 kV, 60 kV and 100 kV as most effective for performing material decomposition with a deviation of 0.28 (0–1.07) mg/ml. The feasibility of our voxelwise analyses using the proposed algorithm was then confirmed by the generation of phantom parameter-maps that matched the known contrast material concentrations. The results were mostly influenced by the noise-level and the concentrations used in the phantoms.

* Corresponding author.
E-mail address: andrea.kronfeld@unimedizin-mainz.de (A. Kronfeld).

https://doi.org/10.1016/j.heliyon.2023.e23013
Received 30 March 2023; Received in revised form 23 November 2023; Accepted 23 November 2023
Available online 6 December 2023

MECT using a standard micro-CT combined with a matrix inversion method is feasible at four different imaging energies and allows the differentiation of mixtures of up to four contrast materials plus an additional residual material.

1. Introduction

Computed tomography (CT) has become indispensable in modern diagnostic imaging due to its widespread availability, high speed, non-invasiveness as well as cost-effectiveness [1]. Technically, the degree of the absorption of radiation generated in the X-ray tube is tissue-specific. Thus, the trans illumination of a body from one direction leads to a summation image of the attenuations of different tissues. Acquisition of many such images from different spatial directions allows generation of cross-sectional images by mathematical reconstruction [2,3].

Technical developments resulted in the introduction of Dual-Energy Computed Tomography (DECT), which years ago has made its way into clinical routine scan protocols [4,5]. Briefly, by using two different energies, tissues, materials or contrast agents can be differentiated due to their particular absorption behavior at different energy levels. Consequently, substances that would be indistinguishable in single energy CT may be distinguished in DECT [6]. Therefore, DECT offers advantages, for example in imaging using iodine-containing contrast agents, in the evaluation of post-interventional intracranial hemorrhage and classification of uric acid versus non-uric acid urinary stones. It has also been successfully applied to reduce periprosthetic metal artifacts [7–10].

In the mid-70s, Alvarez and Macovski have already proposed the theoretical basics for Multi-Energy Computed Tomography (MECT) based on spectral measurements [13]. With novel hybrid pixel detectors and photon-counting CT-scanners, MECT has become an emerging technology in which two or more energies are used for multiple material decomposition [11,12]. This, for example, offers multiple contrast agent imaging, reduction of beam-hardening artifacts or the differentiation of various tissues within one sample [11, 14]. But it is not only further developments in hardware that allow multi-material dissections. Innovations in image processing also open up new avenues: Xue et al. and other working groups have shown that multi-material decomposition is also possible under certain circumstances based on DECT or even single energy data [15–20].

Since years, micro-computed tomography (micro-CT) has been widely used in pre-clinical research providing high-resolution imaging of small and very small structures, and thus is frequently used for non-destructive material testing and small animal imaging.

For the use in small animal micro-CT trials, MECT, however, has been hitherto unexploited. Only a few specialized detectors are available and first in-vivo applications in mouse-models have been published recently [22–24]. With different contrast agents at hand [25–30], MECT is of highest interest not only for clinical, but also for preclinical imaging and non-destructive material analyses. To further demonstrate the potential and broaden the applicability of this technique, we investigated whether MECT can be performed using a standard micro-CT (i.e. non-photon counting and non-spectral detector) combined with a matrix inversion method.

2. Material and methods

2.1. Multi-energy decomposition

Besides the energy of the passing through X-rays, the effective signal intensity *SI* of a CT-voxel depends on the volume fraction and the mass of each contained material as well as on their mass attenuation coefficient. Assumed that the volume fraction sums up to 1, *SI* for a combination of *m* different materials can be described as

$$SI \triangleq \sum_{n=1}^{m-1} \left(\frac{\mu}{\rho}\right)_n \rho_n f_n + \left(1 - \sum_{n=1}^{m-1} f_n\right) \left(\frac{\mu}{\rho}\right)_m \rho_m \qquad 1$$

[31]

For CT-measurements at $e=m-1$ different energies with a known $SI_{pure\ m}$ for $m-1$ materials, this equation can be solved by matrix inversion, and the volume fractions f_1 to f_m can be determined as follows:

$$\begin{bmatrix} f_1 \\ \vdots \\ \vdots \\ f_m \end{bmatrix} = \begin{bmatrix} SI_{pure\ 1,energy\ 1} & \cdots & SI_{pure\ m-1,energy\ 1} \\ \vdots & \ddots & \vdots \\ SI_{pure\ 1,energy\ e} & \cdots & SI_{pure\ m-1,energy\ e} \\ 1 & \ldots & 1 \end{bmatrix}^{-1} \begin{bmatrix} SI_{mix\ energy\ 1} \\ \vdots \\ SI_{mix\ energy\ e} \\ 1 \end{bmatrix} \qquad 2$$

Practically, it is possible to separate $m-1$ different materials plus one residual using $m-1$ different energies.

2.2. Simulation studies to determine the optimal micro-CT protocol

Simulations on virtual phantoms and contrast materials using an in-house MATLAB code (MATLAB 2022b, TheMatWorks, MA, USA) were performed prior to micro-CT measurements in order to cover a broader range of measurements without dissipating our micro-CT's capacity. Virtual phantoms at a volume of five volume units (VU) and up to four different simulated contrast materials

(iodine (I), barium (Ba), gadolinium (Gd) and iron (Fe)) were created, covering all possible combinations of the four contrast materials (CM) with different CM-fractions (0.0 VU, 0.25 VU, 0.5 VU, 0.75 VU and 1.0 VU) for each CM. The volume of each virtual phantom was filled up to five units with water, resulting in total of up to five different materials per virtual phantom. A total number of 625 different virtual phantoms was created. To determine the resulting overall attenuation of each phantom, i.e. the virtual gray value, the phantoms were virtually imaged (i.e. calculated) by multiplication of the different CM-fractions with their dedicated mass attenuation coefficients at the simulated monochromatic energy levels of 30 keV, 40 keV, 50 keV, 60 keV, 80 keV and 100 keV (Table 1) and subsequent addition. For all 15 possible four-out-of-six permutations a random factor was added to the virtual gray values to simulate noise. Its value was chosen to match realistic signal-to-noise (SNR)-levels derived from phantom measurements (Table 1).

The CM-fraction was then re-calculated based on the virtual gray values using Eq. (3) for. The preassigned and the calculated CM-fraction were compared for each virtual phantom, and the error was defined as the absolute value of the difference between the preassigned and the calculated volume fraction including the volume fraction of 0.0 VU (absolute error). A Kruskal-Wallis test was then used to verify a statistical dependence of the results on the particular energy combination and a Wilcoxon rank-sum test to detect possible significant statistical differences between the results for each energy combination on a significance level of 0.05. This was repeated for 1000 different random noise-factors to simulate 1000 measurements. The results were averaged.

Based on these simulations, an optimal energy combination was determined. For the optimal energy combination, firstly, the influence of noise was determined and secondly, the errors for each CM at different volume fractions as well as for different CM-combinations were described. Overall, 1000 measurements were performed on 625 phantoms made from 4 different CM at 15 different permutations which resulted in 37.500.000 single values to be compared to their true value.

2.3. Phantom scans using the micro-CT

Eppendorf tubes (Eppendorf Safe-Lock Tubes, 2.0 ml, Eppendorf AG, Hamburg, Germany) were filled with different solutions containing iodine, barium, gadolinium or iron (Imeron® 400 mg/ml -Iod, Bracco Imaging Deutschland GmbH, Konstanz, Germany; Micropaque ® 1 mg/ml -Barium, Guerbet GmbH, Sulzbach, Germany; Gadovist® 604 mg/ml – Gadolinium, Bayer Vital GmbH, Leverkusen, Germany; Ferro Sanol® 20 mg/ml - Iron, UCB Pharma GmbH, Monheim am Rhein, Germany) in various concentrations and combinations. The solutions were gelled by adding 2 % agarose to avoid motion artifacts from air bubbles during the micro-CT rotation. Phantoms containing a combination of iron and barium could not be prepared, as they chemically reacted to barium ferrate and precipitated. All mixtures and concentrations of the materials in the different phantoms are shown in Fig. 1.

For our imaging studies, an industrial X-ray inspection system (Fig. 2) was used (Yxlon Cheetah; Yxlon International GmbH, Hamburg, Germany). The system contains a cone beam X-ray source equipped with a multifocus X-ray tube allowing operation in a microfocus, nanofocus or high-power mode. A hairpin-filament with a diameter of 200 μm was used to produce a voltage-dependent electron beam of 10 μm–100 μm width, which is focused onto a diamond-like carbon-coated tungsten/beryllium transmission target, resulting in a spot size of less than 1 μm. The opening angle of the beam was 10°. Both, current and voltage were freely selectable. This enables the generation of acceleration voltages of 30 kV–160 kV in steps of 1 kV, which in turn allows the exertion of multi-energy experiments. The anode current is freely adjustable from 1 μA to 1000 μA in 0.1 μA steps. Depending on the focus size, the current is limited by the device itself.

The system featured a 16-bit direct digital flat panel detector (1616 Amorphous Silicon Digital X-ray Detector; Varex Imaging) with a maximum acquisition rate of 24 frames per second (fps) in a 1 × 1 mode (i.e. unbinned scanning mode; pixel matrix of 1280 × 1280) and a pixel pitch of 127 μm^2 (3.94 line pairs/mm). The scanner theoretically provides X–Y feature recognition down to 350 nm and a geometric magnification level of up to 3000 × .

Cone beam-CT-functionality was achieved by rotating the phantoms in the X-ray beam between the X-ray source and the flat panel detector.

For image acquisition, the phantoms were placed in a 3D-printed phantom holder and clamped in the three-jaw chuck of the micro-CT. 720 projections were acquired during one 360° rotation of the phantom holder at an imaging frequency of 8 fps and 6 averages, which resulted in a iteration time of the detector of 750 ms. The anode current was adapted to obtain similar gray values for every acceleration voltage, typically around 250–300 μA at 30 kV and 8–15 μA at 100 kV. A calibration of the detector was performed prior to each measurement. Scans were performed at acceleration voltages of 30 kV, 40 kV, 50 kV, 60 kV, 80 kV and 100 kV. Filtered back projection was used to reconstruct images with an isotropic voxel size of 0.07 × 0.07 × 0.07 mm^3 in a 1260 × 1260 x 1260 matrix.

Table 1
Values at different energies used for simulations.

Energy [keV]	Attenuation coefficient [μ/ρ] [32]				SNR
	Iodine	Barium	Gadolinium	Iron	
30	8.561E+00	9.904E+00	1.484E+01	8.176E+00	215
40	2.210E+01	2.457E+01	6.920E+00	3.629E+00	310
50	1.232E+01	1.379E+01	3.859E+00	1.958E+00	320
60	7.579E+00	8.511E+00	1.175E+01	1.205E+00	310
80	3.510E+00	3.963E+00	5.573E+00	5.952E-01	265
100	1.942E+00	2.196E+00	3.109E+00	3.717E-01	225

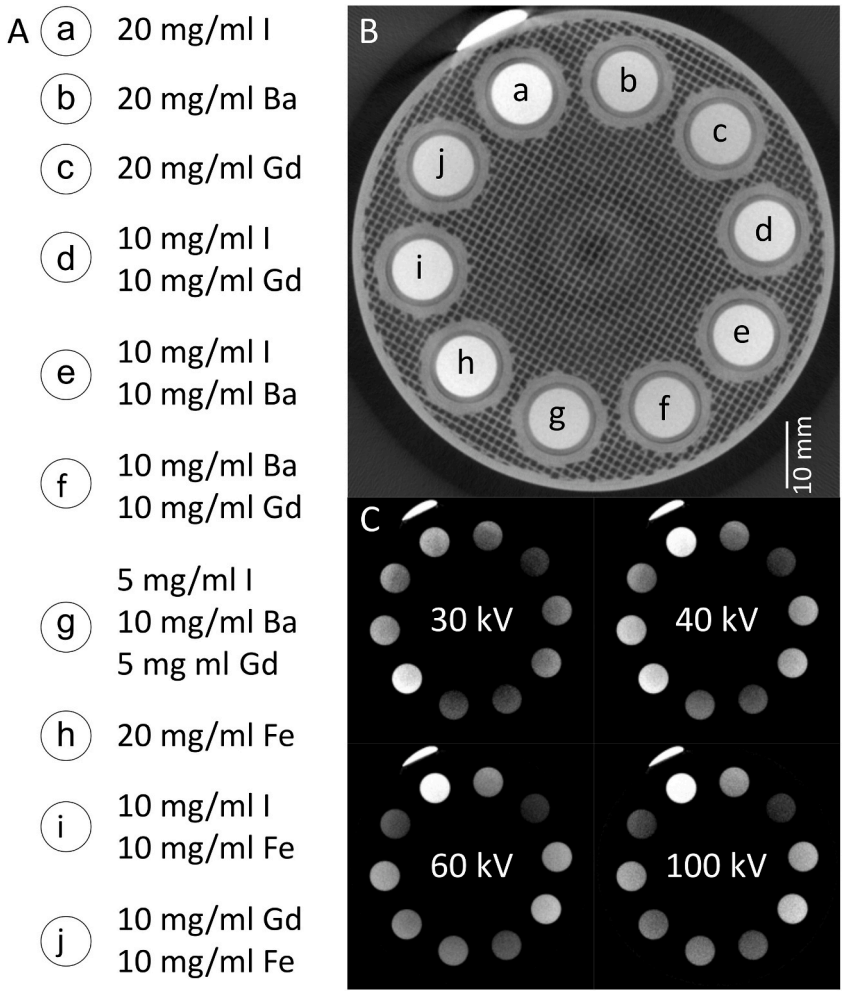

Fig. 1. Phantoms for the Phantom Study: Phantoms with associated contents (A) and their position in the phantom holder (B). Exemplary representation of the sectional, scaled images of the optimal acceleration voltages used (C).). (I: Iodine, Gd: Gadolinium, Ba: Barium, Fe: Iron).

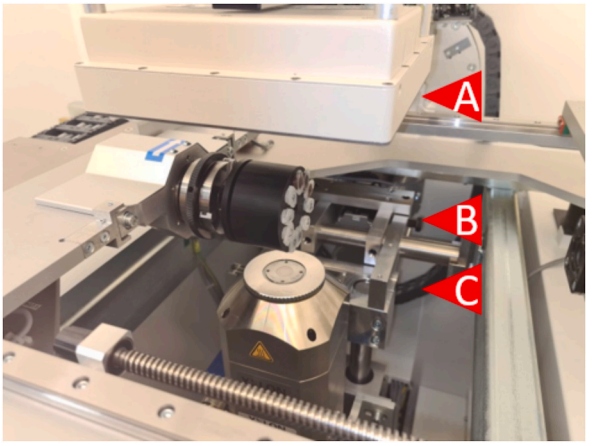

Fig. 2. Experimental setup: Phantom holder equipped with Eppendorf-Tubes clamped in the three-jaw chuck of the industrial micro-CT at the time of the examination. The detector (A) is above the working position to provide a view of the phantom holder (B). The X-ray-tube is positioned below with the transmission target visible (C).

2.4. Material decomposition using a matrix inversion algorithm

The micro-CT data sets were saved and exported in a DICOM-format. For a region of interest (ROI)-based evaluation, ROIs were placed in each phantom in an area showing no inhomogeneities (e. g. air bubbles). The mean signal intensity of every ROI was analyzed using the evaluation algorithm as indicated in Eq. (3). To provide reference values for SI_{pure} for every energy, ROIs were placed only in phantoms containing a single CM of known concentration. The voxel data was filtered by a Gaussian filter ($\sigma = 1$) and then passed to the evaluation algorithm together with the mean pure signal intensities.

The in-house evaluation algorithm (MATLAB 2022b, TheMathworks, MA, USA, MATLAB-command: inv) solved Eq. (2) for the signal intensity of every single phantom at four different energy levels and the pure signal intensities for every CM at four different energies. It provided the concentration c of every CM and the residual content of the voxel.

$$\begin{bmatrix} c_{CA1} \\ c_{CA2} \\ c_{CA3} \\ c_{CA4} \\ c_{residual} \end{bmatrix} = \begin{bmatrix} SI_{pure\ 1,energy\ 1} & \cdots & SI_{pure\ 4,energy\ 1} \\ SI_{pure\ 1,energy\ 2} & \cdots & SI_{pure\ 4,energy\ 2} \\ SI_{pure\ 1,energy\ 3} & \cdots & SI_{pure\ 4,energy\ 3} \\ SI_{pure\ 1,energy\ 4} & \cdots & SI_{pure\ 4,energy\ 4} \\ 1 & \ldots & 1 \end{bmatrix}^{-1} \begin{bmatrix} SI_{mix\ energy\ 1} \\ SI_{mix\ energy\ 2} \\ SI_{mix\ energy\ 3} \\ SI_{mix\ energy\ 4} \\ 1 \end{bmatrix} \quad (3)$$

After decomposition of the CM-concentrations for every possible four-out-of-six combination of acceleration voltages, similar to the simulation study, a Kruskal-Wallis test was used to verify a statistical dependence of the results on the particular combination of acceleration voltages and a Wilcoxon rank-sum test to detect possible significant statistical differences between the results for each combination of acceleration voltages on a significance level of 0.01.

The calculated concentrations are compared to the known concentrations by forming the absolute difference given in mg/ml and the relative difference given in % (specified in the supplementary material).

2.5. Calculation of noise and signal-noise-ratio

Whenever noise is specified, it was determined by subtracting the gray values or concentration values of two adjacent layers from each other, dividing the values by the root mean square of 2, and then forming the standard deviation in a region of interest [33]. To calculate the SNR, the average signal of the two layers in the region of interest was divided by the value of the noise.

2.6. Determination of the influence of various interferences on the results

To determine the influence of different conditions of the environment or disturbances on the results, different parameters of the experimental setup were varied to generate different possible measurement conditions. This included an increase of noise, an increase of scattering, significant lower CM-concentrations and the presence of artifacts. The differences of the true and the determined concentrations are given in absolute values to include the errors made, when the true concentration is zero (i. e. including false positives). Figures depicting the relative errors can be found at the supplementary material.

For every comparison, the afflicted and the normal measurements were done in one sitting and thereby under the same conditions (except the measurement of varying concentrations). As a byproduct, the measurements done for comparison could be used to get a rough survey on the reproducibility of our measurements. All measurements were done on concentration maps derived from the optimal acceleration voltages with an detector iteration time of 750 ms and evaluated using Gaussian filtering with $\sigma = 1$ (unless otherwise noted) and for voxel containing phantom material.

2.6.1. Noise

To determine the influence of the noise, images with different noise levels were generated at the previously determined four optimal energies. For this purpose, the time of data iteration of the detector was set to 125 ms, 375 ms and 750 ms. As a control, the noise and SNR were determined in the manner described above and the concentrations of the different test substances in each phantom were determined for all 3 iteration times and compared to the true concentrations.

Another way to influence the noise is to increase the filtering of the raw images. To determine the influence of filtering, Gaussian smoothing with $\sigma = 1$, $\sigma = 3$ and $\sigma = 6$ was applied to the unprocessed images.

2.6.2. Scattering

To vary the scattering, the distance between the X-ray tube and detector was increased from 264 mm to 329 mm (25 %), but the image geometry was preserved so that the magnification remained constant. In addition, the image intensity was adjusted via the tube current so that it was constant for all measurements. For this, the current had to be increased between 6 μA at 100 kV and 73 μA at 30 kV. This caused an increase in the scatter due to the increased distance between the X-ray tube and the detector but no major change in SNR. Again, the true and calculated contrast material concentrations were compared for the two different distances between the X-ray tube and detector.

2.6.3. Artifacts

A metal pin was inserted into the center of the phantom holder, which produced radial beam hardening artifacts. The concentrations of the contrast materials were calculated in the presence and absence of artifacts and compared with the true concentrations.

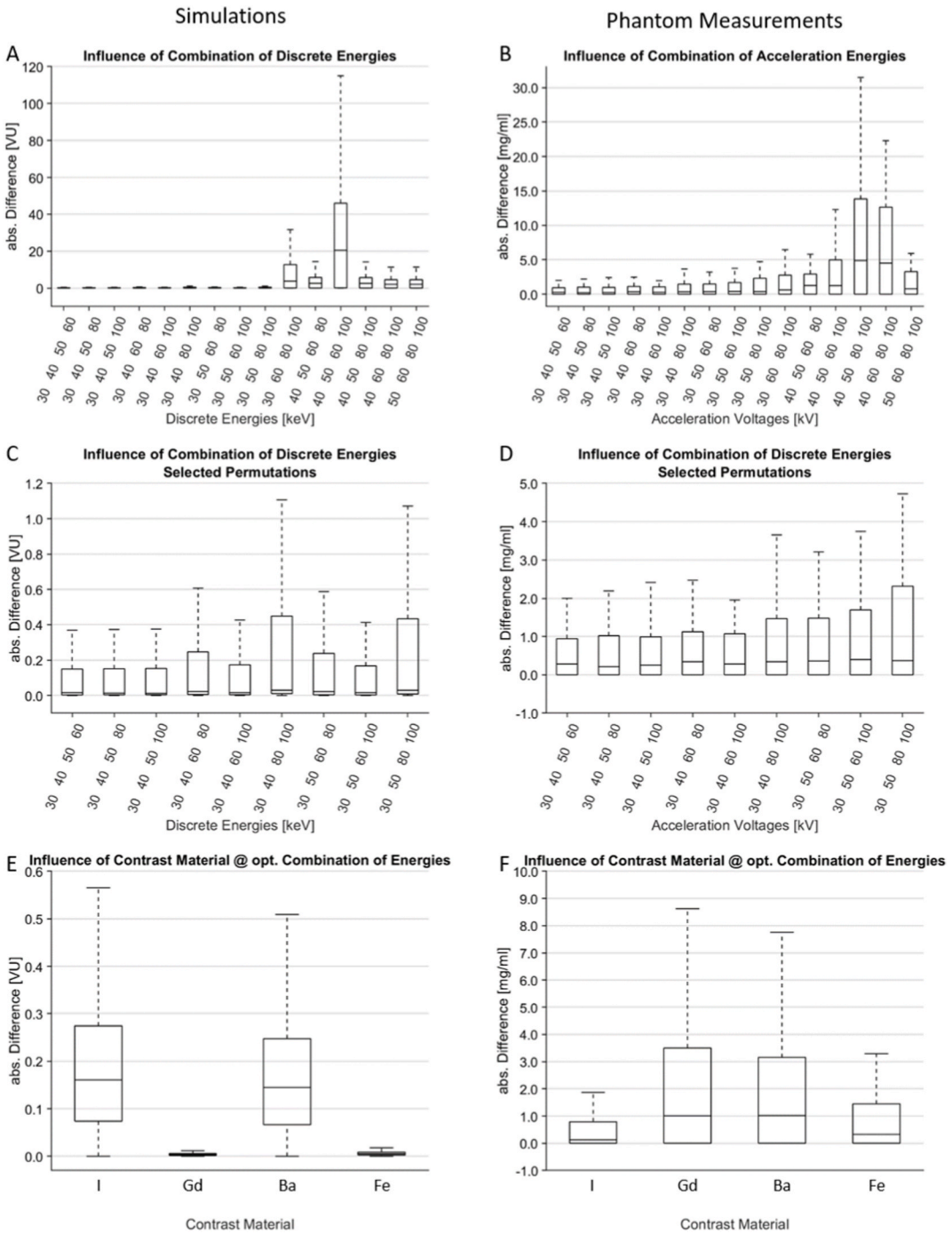

Fig. 3. Determination of the Optimal Energy/Voltage: Comparison of the results of simulation and phantom study: A and B show the influence of the energy permutation/the acceleration voltages on the absolute difference between the known and the calculated concentration given in volume units (VU) for the simulations and absolute values for the phantom measurements. In C and D, for a better visualization, selected permutations with smaller differences are magnified. In E and F, the differences are itemized for the different CM. On each box, the central line indicates the median, and the bottom and top boundary of the box indicate the 25th and 75th percentiles, respectively. The whiskers extend to the most extreme data points not considered outliers, outliers are not shown.). (I: Iodine, Gd: Gadolinium, Ba: Barium, Fe: Iron).

2.6.4. Lower CM-concentrations

To estimate the influence of contrast material concentration on the accuracy of the method, the experiment was repeated using phantoms with 20 % of the initial concentration (i.e., maximum 4 mg/ml) of contrast materials. The true and calculated concentrations were compared and contrasted with the results obtained with phantoms of high concentration from the noise-measurements with an iteration time of 750 ms.

2.6.5. Reproducibility

As a by-product of the previous measurements, the reproducibility of the method over several days could be determined from the comparison images. For this purpose, the variation of the deviations of the calculated from the true concentration values was given.

2.7. Determination of recognition-rates

Considering true positive or false negative voxels gives a good impression of the binary identification of the algorithm. The recognition rates were calculated for all CM using the following formulas, whereby the threshold above which a voxel was classified as "containing CM" was defined as 1 % of the median SI in the air outside the phantom holder.

$$TPR = \frac{TP}{TP + FN} + 100\% \quad \text{Eq. 4a}$$

$$TNR = \frac{TN}{TN + FP} + 100\% \quad \text{Eq. 4b}$$

$$FPR = \frac{FP}{FP + TN} + 100\% \quad \text{Eq. 4c}$$

$$FNR = \frac{FN}{FN + TP} + 100\% \quad \text{Eq. 4d}$$

(TPR: true positive rate, TP: true positive, TNR: true negative rate, TN: true negative, FPR: false positive rate, FP: false positive, FNR: false negative rate, FN: false negative).

The calculation of the four values was done on concentration maps from the optimal acceleration voltages with an detector iteration time of 750 ms and evaluated using Gaussian filtering with $\sigma = 1$ and for voxel containing phantom material.

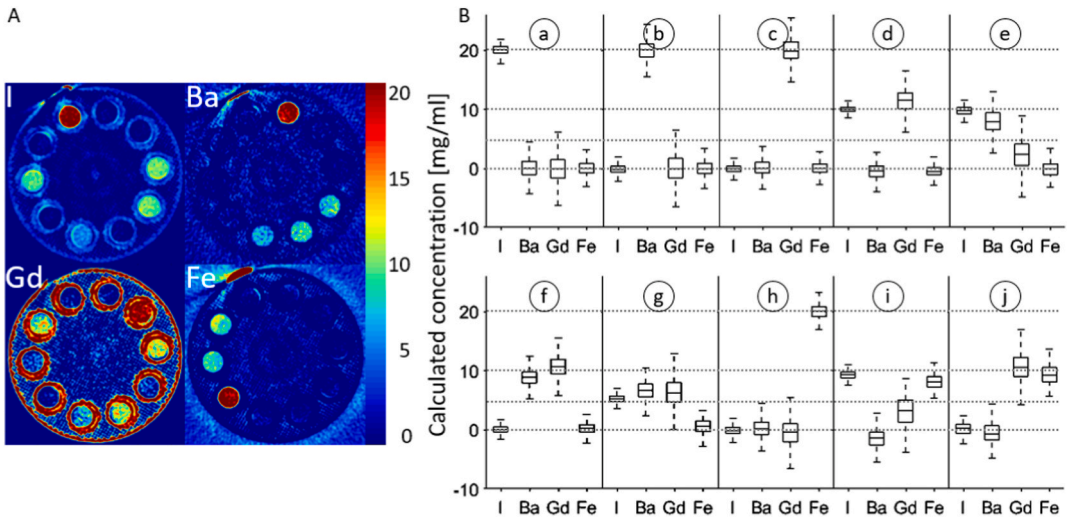

Fig. 4. Voxelwise evaluation: Calculated fraction maps of the different CM (Gaussian filtering with $\sigma = 3$). (A) Reflect the results of the ROI-based evaluation. (B) True and calculated concentration fractions for each phantom. The numbers below the materials and dotted grid lines depict concentrations of 5 mg/ml, 10 mg/ml and 20 mg/ml. Circled letters correspond to the phantom identification as shown in Fig. 1. On each box, the central line indicates the median, and the bottom and top boundary of the box indicate the 25th and 75th percentiles, respectively. The whiskers extend to the most extreme data points not considered outliers, outliers are not shown.). (I: Iodine, Gd: Gadolinium, Ba: Barium, Fe: Iron).

3. Results

3.1. Simulated material decomposition

The Kruskal-Wallis test showed a statistical dependence of the results on the particular combination of simulated energies ($p \ll < 0.01$). The smallest median absolute difference was reached when combining 30 keV, 40 keV, 50 keV and 100 keV with 0.01 (0.003–0.15) VU, which does not differ significantly from the differences caused by the energy-combinations number 1, 2, 5 and 8 (Sup. 1). The absolute errors for each individual CM showed differences with remarkable lower error values for Gd and Fe: I 0.16 (0.07–0.27) VU, Gd 0.003 (0.002–0.006) VU, Ba 0.14 (0.07–0.25) VU and Fe 0.005 (0.002–0.009) VU (median (25 %–75 %)) (Fig. 3 E, Sup. 2). The error for the 15 different four-out-of-six combinations of acceleration energies is shown in Fig. 3 A and C.

A variation of noise from 0.1 times to twice the original noise resulted in a linear decrease and increase of the error, respectively. Moreover, we did not observe an error-dependence on the different volume fractions or mixtures of CM.

3.2. Phantom measurements using the micro-CT

The ROI-based phantom evaluation showed comparable characteristics to the simulation evaluation including a significant dependence from the combination of acceleration voltages, albeit slightly shifted to higher energy levels. The differences between the known and the calculated concentrations are small as long as 30 kV, 40 kV and either 50 kV or 60 kV are included into the combination of acceleration voltages. The minimal difference was determined when combining acceleration voltages of 30 kV, 40 kV, 60 kV and 100 kV with a median of 0.28 (0–1.07) mg/ml overall (Fig. 3 B and D) and 0.13 (0–0.79) mg/ml for I, 1.01 (0–3.50) mg/ml for Gd, 1.02 (0–3.15) mg/ml for Ba and 0.33 (0–1.45) mg/ml for Fe (median (25 %–75 %)) (Fig. 3 F, Sup. 2). As in the simulation study, the results for this combination of acceleration voltages shoes no significant difference to the surrounding combinations (Sup. 1).

The voxel wise evaluation at the optimal energy combination derived from the ROI-based phantom evaluation provided an overview of the expected appearance of MECT-parameter maps. In contrast to the preceding result of the simulation study, a mutual influence of the different CM was visible, especially in phantom g, where three CMs were combined. We moreover noticed, that the concentration of Ba was frequently underestimated, whereas the concentration of Gd was frequently overestimated (Fig. 4 B).

3.3. Influence of various interferences on the results

3.3.1. Noise

By varying the time of data iteration of the detector from 125 ms to 750 ms, the noise could be approximately bisected (Sup. 3 B). This led to a reduction of the differences between the known and the calculated concentrations of more than 50 % for all CM (Table 2, Fig. 5 A, Sup. 3 A). Smoothing the raw images by Gaussian filtering leads to an exponential decay of the noise values (Sup. 3 D). The differences in concentration are following this exponential pattern and are reduced from $\sigma = 1$ to $\sigma = 6$ for all CM (Table 2, Fig. 5 B, Sup. 3 C).

3.3.2. Scattering

It was possible to increase the distance between the X-ray-source and the detector by 25 % with only minor changes of the signal intensities and noise by increasing the anode current (Sup. 3 F). The remaining influences by the increased scattering only led to small changes of the differences between the known and the calculated concentrations (Table 2, Fig. 5C, Sup. 3 E).

3.3.3. Artifacts

The metal pin in the center of the phantom holder lead to moderate beam hardening artifacts (Sup. 4 E and F). The high signal intensity of the metal pin led to an adjustment of the total image intensity during the reconstruction. This reduced the signal intensity

Table 2
Absolute values of differences between known and calculated concentration given in mg/ml as median (interquartile range) unless otherwise stated.

		Iodine		Gadolinium		Barium		Iron	
Noise	125 ms	6.19	(7.61)	24.81	(30.65)	16.19	(19.96)	10.91	(13.41)
	375 ms	3.64	(4.49)	14.80	(18.22)	9.52	(11.74)	6.52	(8.05)
	750 ms	2.60	(3.20)	10.04	(12.39)	6.63	(8.19)	4.55	(5.60)
Gauss	$\sigma = 1$	2.60	(3.20)	10.04	(12.39)	6.63	(8.19)	4.55	(5.60)
	$\sigma = 3$	0.84	(1.04)	3.66	(4.55)	2.37	(2.90)	1.77	(2.29)
	$\sigma = 6$	0.43	(0.53)	2.23	(2.99)	1.45	(1.82)	1.11	(1.66)
Scattering	higher	3.51	(4.32)	14.05	(17.36)	9.23	(11.37)	6.18	(7.63)
	lower	3.54	(4.38)	14.73	(18.15)	9.39	(11.58)	6.55	(8.07)
Artifacts	with	3.04	(3.75)	11.68	(14.43)	7.68	(9.48)	5.10	(6.28)
	without	2.70	(3.33)	10.09	(12.67)	6.82	(8.43)	4.53	(5.61)
Concentrations	max. 4 mg/ml (abs.)	2.04	(2.52)	9.49	(11.70)	8.38	(10.35)	3.64	(4.48)
	max. 20 mg/ml (abs.)	2.60	(3.20)	10.04	(12.39)	6.63	(8.19)	4.55	(5.60)
	max. 4 mg/ml (rel. [%])	85.77	(115.1)	392.0	(512.6)	320.9	(431.8)	147.0	(183.3)
	max. 20 mg/ml (rel. [%])	25.14	(34.68)	80.40	(107.6)	54.37	(72.44)	43.66	(67.10)

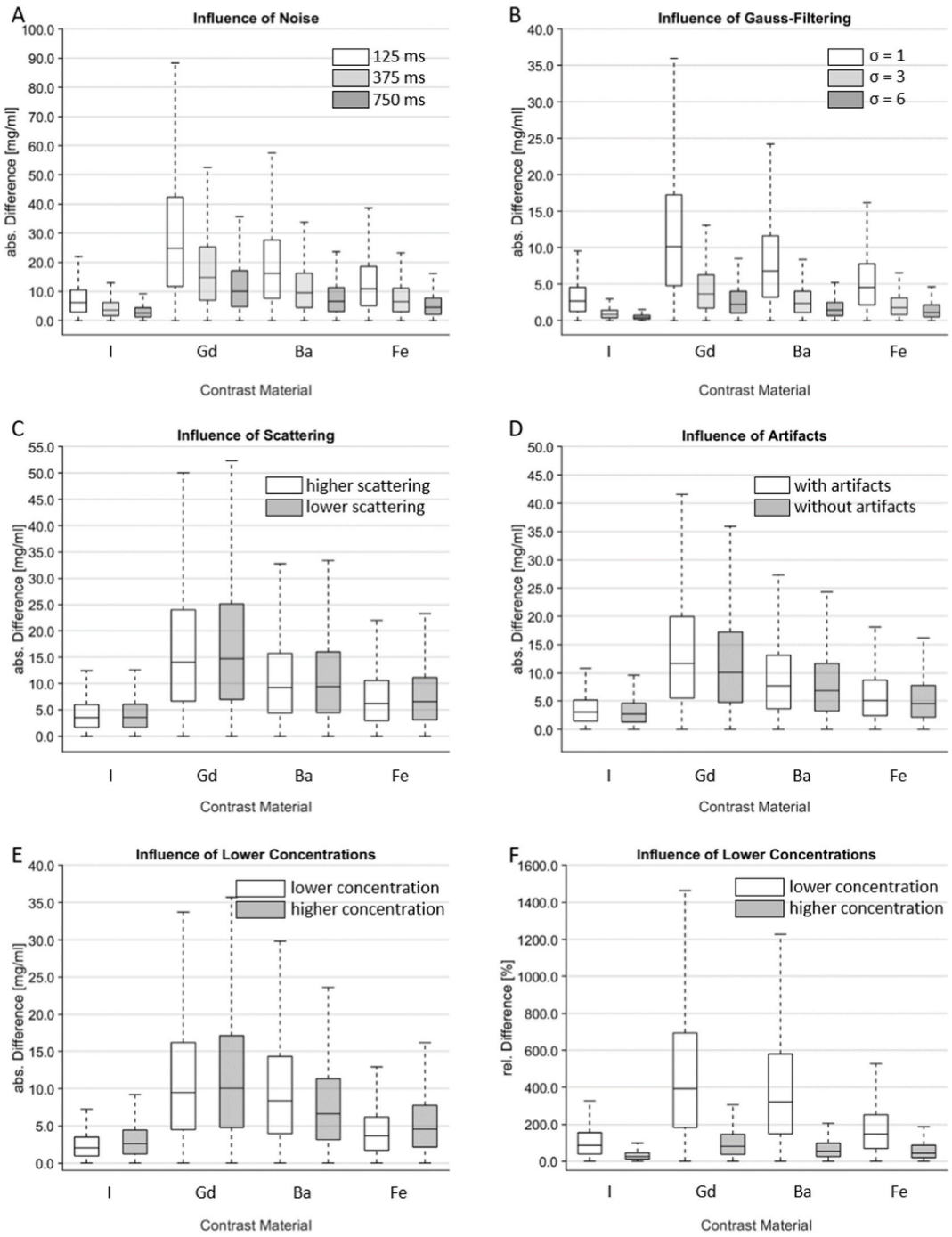

Fig. 5. Influences of different changes of the measurement and evaluation environment: The increase of integration time of the detector and thus the decrease of noise reduces the differences between the known and the calculated concentrations (A). (B) Shows the similar effect of increasing Gaussian filtering. Increased scattering (C) and the presence of artifacts (D) have no major effect on the differences. Lower CM (contrast material)-concentrations do not lead to higher absolute differences (E) but strongly increase the relative difference (F). (I: Iodine, Gd: Gadolinium, Ba: Barium, Fe: Iron).

within the phantoms by about 1/3, but also reduced the noise by about the same amount (Sup. 4 C and D). This leads to a comparable SNR and also comparable differences between the known and the calculated concentrations with and without artifacts (Table 2, Fig. 5 D, Sup. 4 A and B).

3.3.4. Lower CM-concentrations

Even after reducing the CM concentrations to 1/5 of the initial concentrations (maximum concentration 4 mg/ml), it was possible to break down the gray values into the different CM. The absolute differences between known and calculated concentrations were comparable to those of measurements with high concentrations (Table 2, Fig. 5 E). However, looking at the relative differences gives a better impression. Here it can be seen that the differences in the case of low concentrations are on average about 4 times the values of the differences in the case of high concentrations (Table 2, Fig. 5 F).

3.3.5. Reproducibility

The reproducibility of the signal intensities within the phantoms was good over 4 different measurement days. However, the noise differs by up to 30 %–40 %. This leads to deviations in the concentration differences of over 30 % in the case of Fe and Ba but better deviations for I and Gd (Sup. 5).

3.4. Recognition rates

The recognition-rates were determined for every CM following Eq. 4a-d (Table 3, Fig. 6).

4. Discussion

Micro-CT has become a mainstay of modern, non-invasive laboratory small animal imaging as it yields optimized insights into different pathologies, allows the evaluation of novel therapeutic strategies and mainly underpins the 3R-principle (i.e. refinement and reduction). The 3R principle represents the most important ethical principle in experimental animal research. Consequently, micro-CT has been utilized for a vast range of applications such as imaging of mouse brain vessels [34], bony structures [35], tumors [36], contrast agent development [37] and many others [21]. Focusing on MECT using micro-CT, only a limited number of studies has been performed hitherto. Whereas in almost all studies micro-CT were equipped with highly specialized spectral detectors, photon counting detectors, or dedicated X-ray sources [38–43], to our best knowledge, no such MECT studies using a conventional micro-CT exist.

As indicated above, spectral detectors such as the medipix3 and the DECTRIS detector allow MECT [14,22–24,44–46]. This type of detector, for example, is able to detect and count individual particles that hit each detector pixel. Thus, this detector is both energy-resolving and photon-counting and thereby allows quantitative imaging. In our case, a normal energy-integrating detector (EID) is used in our experiments, and consequently, the detected signal is proportional to the total energy deposited by all photons without neither specific information regarding individual photons and their energy nor relevant spectral information. To differentiate between different CM using an EID, the energy levels as well as their number (depending on the number of CM to be differentiated) must be known in advance. The disadvantage is given by the fact, that the more spectral information is required, the more often an object hast to be imaged at another energy level. One workaround to reduce the problem of multiple scans for MECT with EIDs has been recently published by Ren et al. who mounted a z-axis split-filter (0.05 mm Au, 0.6 mm Sn) on one tube of a dual-source EID CT scanner [42,43]. With the two split X-ray beams from the first tube and the third beam from the second tube, they were able to acquire different X-ray spectra with three beams simultaneously and were able to distinguish three contrast materials (I, Gd, Bi plus water). In our experiments using an EID even four different contrast materials (plus residual non-contrast material) were differentiated.

A drawback of our setup is the fact that a) increased radiation doses are required due to repeated scans at different energy levels and b) problems in material decomposition may arise from movements when scanning living animals repetitively. Therefore, photon counting or multi-source-CT may preferably be used in preclinical MECT imaging. However, by far, these scanners are not ubiquitously available. The experimental approach described herein may help to bridge the gap until photon-counting CT-scanners (also in small animal imaging) will be available and hence MECT-experiments at lower radiation doses are feasible.

X-ray imaging normally relies on energy spectra. This becomes apparent, when comparing our simulations to the micro-CT-based phantom measurements. Although the micro-CT measurements generally confirm the results of the simulations, we observed a slight shift towards higher energy levels when using the micro-CT. This may be explained by the fact, that the selected acceleration voltage represents only the highest energy of a continuous spectrum of X-rays. Whereas our simulations were based upon discrete (i.e. virtually monochromatic) energy levels (30 keV, 40 keV, 50 keV, and 100 keV) the continuous spectrum of X-rays used in our micro-CT experiments also included X-rays at lower energy levels, which may have caused this shift towards slightly higher acceleration voltage levels (30 kV, 40 kV, 60 kV, and 100 kV) to reach comparable results. Both, simulation as well as phantom experiments suggest optimal results if two lower, one mid and one high energy/acceleration voltage are included into the combination. Regarding the attenuation coefficients of the different CM, it is striking, that the k-edges of the materials are located in the lower and the middle energy-ranges (Fig. 7). The different relations of signal intensities at the different energies/acceleration voltages enable the decomposition-algorithm to work optimally and produce the best results. The contrast materials as well as their required concentrations can be considered prior to animal experiments, hereby supporting the 3R-principle.

Table 3
TPR and FNR of the four CM.

	Iodine	Gadolinium	Barium	Iron
TPR	98.1 %	81.4 %	84.2 %	83.4 %
FNR	1.85 %	18.6 %	15.8 %	16.6 %

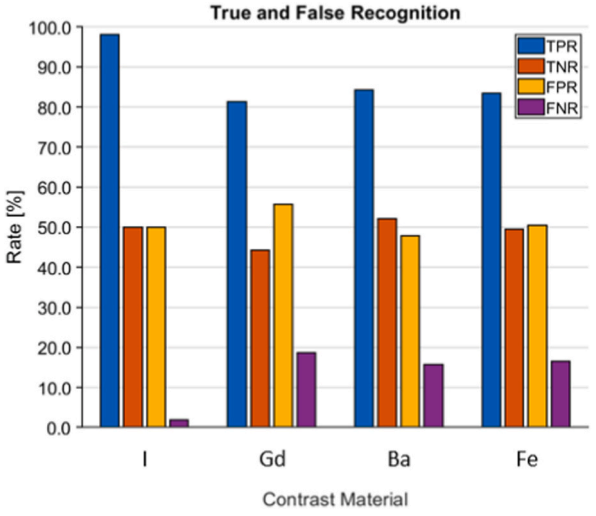

Fig. 6. True and false recognition rates: True and false recognition rates given in % for every CM (contrast material; TPR: true positive rate, TNR: true negative rate, FPR: false positive rate, FNR: false negative rate).

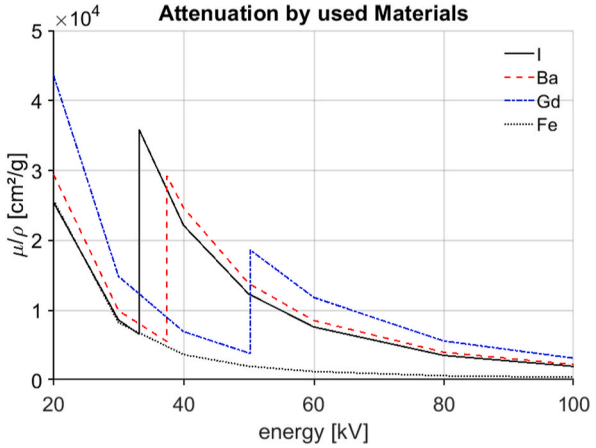

Fig. 7. Attenuation Curves: Attenuation curves of the different contrast materials by energy show a similar trend for I (Iodine) and Ba (Barium) with slightly different k-edges, whereas the attenuation curves of Gd (Gadolinium) and Fe (Iron) differ from those of I and Ba, as well as from each other.

Interestingly, in our simulations, typical MRI-contrast materials such as Gd and Fe that are rarely used in CT-imaging showed a superior quantifiability with a minimal error compared to typical CT-contrast materials such as iodine and barium (Fig. 3E). This is most probably due to the more suitable attenuation characteristics that depend on the applied energy. Whereas iodine-based and barium-based CMs showed very similar attenuation curves, the curves of each gadolinium and iron differ and can be differentiated more easily at optimal maximum energy levels (Fig. 7). Moreover it is notable, that the best results can be achieved, if 30 kV and 40 kV are enclosed in the evaluation. This can be explained by energy levels of the k-edges of I and Ba in the spectrum below 40 kV, which covers that range well [47]. In the range of the energy spectrum below 30 kV the attenuation coefficient of Gd differs significantly from the other attenuation coefficients, which improves the separation of Gd as well as the k-edge of Gd in the energy range below 60 kV. Fe does not exhibit a k-edge in the whole chosen energy spectrum which makes it well separable from the other CM. When comparing the quantifiability of contrast materials in real CT phantom scans (Fig. 3F), however, the advantage of Fe and Gd does no longer exist. This is most probably is due to the applied continuous spectrum of X-ray.

The voxelwise evaluation can give an idea of how MECT-*in vivo* experiments may look like and which quantification accuracy one may expect.

The investigations of the further influences on the accuracy of the method show that the optimization of the noise or the SNR is indispensable for the realization of the method. Besides the possibility to influence the image quality already during the image acquisition (e.g. by increasing the number of averages or the duration of signal collection), the noise of the output data can also be positively influenced afterwards by suitable filtering. Both methods have their advantages and disadvantages, which are less important

in our phantom study than they would be in a preclinical study in small animals: Longer acquisition times can lead to problems or errors in the calculation of CM concentrations in the living animal due to respiration, heartbeat or even rapid removal processes of the CM. Filtering during post-processing of the images does not affect the duration of the measurement, but can lead to a loss of small details and spatial resolution. Here it is necessary to take care that the filtering is adapted to the details that are investigated (e. g. moderate filtering, edge-preserving). A solution here can be a suitable combination of optimization of image acquisition and filtering in post-processing. Another improvement might also be achieved with post-processing based on neural networks. However, it must be ensured that the gray values are not changed, so that the calculated concentrations are not distorted.

TPR and FNR are very good for iodine and acceptable for the other three CM (Table 3). However, the values for TNR and FPR are each around 50 % (Fig. 6). This means that only 50 % of the voxels that actually do not contain CM are recognized as such, or 50 % of the voxels that actually do not contain CM are still recognized as such. All in all, this means that the sensitivity of the method is good, but the specificity is only around 50 %.

To conclude, quantitative MECT using a micro-CT with an energy integrating detector is feasible and can be used for up to four different energy levels. Furthermore, the precedent simulations in our approach may help to confine scan protocols prior to testing. A suitable noise-management is of utmost importance.

Data availability statement

Data will be made available on request.

CRediT authorship contribution statement

Andrea Kronfeld: Writing – review & editing, Writing – original draft, Visualization, Validation, Supervision, Software, Resources, Project administration, Methodology, Investigation, Formal analysis, Data curation, Conceptualization. **Patrick Rose:** Writing – original draft, Validation, Software, Resources, Methodology, Investigation, Formal analysis, Data curation, Conceptualization. **Jan Baumgart:** Supervision, Resources, Project administration. **Carolin Brockmann:** Supervision, Project administration, Conceptualization. **Ahmed E. Othman:** Supervision, Project administration, Conceptualization. **Bernd Schweizer:** Supervision, Project administration, Conceptualization. **Marc Alexander Brockmann:** Writing – original draft, Supervision, Project administration, Investigation, Funding acquisition, Conceptualization.

Declaration of competing interest

The authors declare that they have no known competing financial interests or personal relationships that could have appeared to influence the work reported in this paper.

Acknowledgements

Acquisition of the micro-CT was funded by the German Research Council (Deutsche Forschungsgemeinschaft, DFG; grant INST 371/49-1 FUGG).

Appendix A. Supplementary data

Supplementary data to this article can be found online at https://doi.org/10.1016/j.heliyon.2023.e23013.

References

[1] C. Liguori, et al., Emerging clinical applications of computed tomography. Medical Devices, Auckland, N.Z.) 8 (2015) 265–278, https://doi.org/10.2147/mder.S70630.
[2] C.C. Ferreira, et al., Total mass attenuation coefficient evaluation of ten materials commonly used to simulate human tissue, J. Phys. Conf. 249 (2010) 12029, https://doi.org/10.1088/1742-6596/249/1/012029.
[3] J. Ambrose, *Computerized transverse axial scanning (tomography): Part 2. Clinical application*, The British Journal of Radiology 46 (552) (1973) 1023–1047, https://doi.org/10.1259/0007-1285-46-552-1023.
[4] S. Faby, et al., Performance of today's dual energy CT and future multi energy CT in virtual non-contrast imaging and in iodine quantification: a simulation study. Medical physics 42 (7) (2015) 4349–4366, https://doi.org/10.1118/1.4922654.
[5] C.H. McCollough, et al., Dual- and multi-energy CT: principles, technical approaches, and clinical applications. Radiology 276 (3) (2015) 637–653, https://doi.org/10.1148/radiol.2015142631.
[6] A. Agostini, et al., Dual-energy CT: theoretical principles and clinical applications. La Radiologia medica 124 (12) (2019) 1281–1295, https://doi.org/10.1007/s11547-019-01107-8.
[7] C. Brockmann, et al., Dual-energy CT after peri-interventional subarachnoid haemorrhage: a feasibility study. Clinical neuroradiology 20 (4) (2010) 231–235, https://doi.org/10.1007/s00062-010-0036-3.
[8] G. Foti, et al., Diagnostic performance of dual-energy CT for detecting painful hip prosthesis loosening, Radiology (2021) 203510, https://doi.org/10.1148/radiol.2021203510.
[9] T.T. Kellock, et al., Detection of bone marrow edema in nondisplaced hip fractures: utility of a virtual noncalcium dual-energy CT application, Radiology 284 (3) (2017) 798–805, https://doi.org/10.1148/radiol.2017161063.

[10] A.N. Primak, et al., Noninvasive differentiation of uric acid versus non-uric acid kidney stones using dual-energy CT, Acad. Radiol. 14 (12) (2007) 1441–1447.
[11] C.H. McCollough, et al., Principles and applications of multienergy CT: report of AAPM task group 291, Medical physics 7 (2020) 47, https://doi.org/10.1002/mp.14157, p. e881-e912.
[12] P. Rajiah, et al., Update on multienergy CT: physics, principles, and applications. Radiographics, a review publication of the Radiological Society of North America, Inc 40 (5) (2020) 1284–1308, https://doi.org/10.1148/rg.2020200038.
[13] R.E. Alvarez, A. Macovski, Energy-selective reconstructions in X-ray computerized tomography, Phys. Med. Biol. 21 (5) (1976) 733–744, https://doi.org/10.1088/0031-9155/21/5/002.
[14] N.G. Anderson, et al., Spectroscopic (multi-energy) CT distinguishes iodine and barium contrast material in MICE. European radiology 20 (9) (2010) 2126–2134, https://doi.org/10.1007/s00330-010-1768-9.
[15] Q. Ding, et al., Image-domain multimaterial decomposition for dual-energy CT based on prior information of material images, Med. Phys. (2018), https://doi.org/10.1002/mp.13001.
[16] Y. Long, J.A. Fessler, Multi-material decomposition using statistical image reconstruction for spectral CT, IEEE Trans. Med. Imag. 33 (8) (2014) 1614–1626, https://doi.org/10.1109/TMI.2014.2320284.
[17] Y. Xue, et al., Accurate multi-material decomposition in dual-energy CT: a phantom study, Ieee Transactions on Computational Imaging 5 (4) (2019) 515–529, https://doi.org/10.1109/Tci.2019.2909192.
[18] Y. Xue, et al., Image domain multi-material decomposition using single energy CT, Phys. Med. Biol. 65 (6) (2020) 65014, https://doi.org/10.1088/1361-6560/ab7503.
[19] Y. Xue, et al., Multi-material decomposition for single energy CT using material sparsity constraint, IEEE Trans. Med. Imag. 40 (5) (2021) 1303–1318, https://doi.org/10.1109/TMI.2021.3051416.
[20] Y. Xue, et al., Statistical image-domain multimaterial decomposition for dual-energy CT, Med. Phys. 44 (3) (2017) 886–901, https://doi.org/10.1002/mp.12096.
[21] S.J. Schambach, et al., Application of micro-CT in small animal imaging. Methods (San Diego, Calif.) 50 (1) (2010) 2–13, https://doi.org/10.1016/j.ymeth.2009.08.007.
[22] D.P. Clark, et al., Photon-counting cine-cardiac CT in the mouse, PLoS One 14 (9) (2019), e0218417, https://doi.org/10.1371/journal.pone.0218417.
[23] M.F. Walsh, et al., Spectral CT data acquisition with Medipix3.1, J. Instrum. (2013) 8, https://doi.org/10.1088/1748-0221/8/10/P10012.
[24] M.F. Walsh, et al., First CT using Medipix3 and the MARS-CT-3 spectral scanner, J. Instrum. (2011) 6. DOI: Artn C01095 10. 1088/1748-0221/6/01/C01095.
[25] P.C. Naha, et al., Dextran coated bismuth-iron oxide nanohybrid contrast agents for computed tomography and magnetic resonance imaging, J. Mater. Chem. B 2 (46) (2014) 8239–8248, https://doi.org/10.1039/C4TB01159G.
[26] J.R. Ashton, et al., Dual-energy micro-CT functional imaging of primary lung cancer in mice using gold and iodine nanoparticle contrast agents: a validation study, PLoS One 9 (2) (2014), e88129, https://doi.org/10.1371/journal.pone.0088129.
[27] J.R. Ashton, J.L. West, C.T. Badea, In vivo small animal micro-CT using nanoparticle contrast agents, Front. Pharmacol. 6 (2015) 256, https://doi.org/10.3389/fphar.2015.00256.
[28] C. Cruje, et al., PEG-modified gadolinium nanoparticles as contrast agents for in vivo micro-CT. Sci Rep 11 (1) (2021) 16603, https://doi.org/10.1038/s41598-021-95716-x.
[29] H. Boll, et al., Comparison of Fenestra LC, ExiTron nano 6000, and ExiTron nano 12000 for micro-CT imaging of liver and spleen in mice, Acad. Radiol. 20 (9) (2013) 1137–1143, https://doi.org/10.1016/j.acra.2013.06.002.
[30] S. Kirschner, et al., In vivo micro-CT imaging of untreated and irradiated orthotopic glioblastoma xenografts in mice: capabilities, limitations and a comparison with bioluminescence imaging. J Neurooncol 122 (2) (2015) 245–254, https://doi.org/10.1007/s11060-014-1708-7.
[31] X. Liu, et al., Quantitative imaging of element composition and mass fraction using dual-energy CT: three-material decomposition, Med. Phys. 36 (5) (2009) 1602–1609, https://doi.org/10.1118/1.3097632.
[32] Hubbell, J.H. and S.M. Seltzer, X-ray mass attenuation coefficients, in NIST Standard Reference Database 126. 2004, Radiation Physics Division, PML, NIST DOI: 10.18434/T4D01F.
[33] X.Y. Tian, E. Samei, Accurate assessment and prediction of noise in clinical CT images, Med. Phys. 43 (1) (2016) 475–482, https://doi.org/10.1118/1.4938588.
[34] V. Weyer, et al., Longitudinal imaging and evaluation of SAH-associated cerebral large artery vasospasm in mice using micro-CT and angiography. Journal of cerebral blood flow and metabolism, official journal of the International Society of Cerebral Blood Flow and Metabolism 40 (11) (2020) 2265–2277, https://doi.org/10.1177/0271678x19887052.
[35] K. Engelke, et al., Mikro-CT. Technologie und Applikationen zur Erfassung von Knochenarchitektur. Der Radiologe 39 (3) (1999) 203–212, https://doi.org/10.1007/s001170050497.
[36] H. Boll, et al., Micro-CT based experimental liver imaging using a nanoparticulate contrast agent: a longitudinal study in mice, PLoS One 6 (9) (2011), e25692, https://doi.org/10.1371/journal.pone.0025692.
[37] T. Henning, et al., Imaging characteristics of DHOG, a hepatobiliary contrast agent for preclinical microCT in mice, Acad. Radiol. 15 (3) (2008) 342–349, https://doi.org/10.1016/j.acra.2007.10.007.
[38] H. Yu, et al., Medipix-based spectral micro-CT. CT Li lun yu ying yong yan jiu 21 (4) (2012) 583.
[39] J.P. Schlomka, et al., Experimental feasibility of multi-energy photon-counting K-edge imaging in pre-clinical computed tomography, Phys. Med. Biol. 53 (15) (2008) 4031–4047, https://doi.org/10.1088/0031-9155/53/15/002.
[40] S. Masetti, et al., Preliminary results of a Multi-Energy CT system for small animals, J. Instrum. (2009) 4. DOI: Artn P06011 10. 1088/1748-0221/4/06/P06011.
[41] M. Moghiseh, et al., Discrimination of multiple high-Z materials by multi-energy spectral CT– A phantom study, JSM Biomed Imaging Data Pap (2016) 3, 1007.
[42] L. Ren, et al., Energy-integrating-detector multi-energy CT: implementation and a phantom study. Med Phys 48 (9) (2021) 4857–4871, https://doi.org/10.1002/mp.14943.
[43] L. Ren, et al., Multi-energy CT with triple X-ray beams: a feasibility animal study, Proc. SPIE-Int. Soc. Opt. Eng. (2020) 11312, https://doi.org/10.1117/12.2549780.
[44] C.R.L. Juan, H. Ian, D. Mini, Tissue classification and contrast agent separation in spectral micro CT using Medipix3 CdTe detector, in: Proc. SPIE PC12031, Medical Imaging, Physics of Medical Imaging, 2022. PC120310N (11 April 2022), https://doi.org/10.1117/12.2613361.
[45] T.E. Kirkbride, et al., Discrimination between calcium hydroxyapatite and calcium oxalate using multienergy spectral photon-counting CT, AJR Am. J. Roentgenol. 209 (5) (2017) 1088–1092, https://doi.org/10.2214/AJR.17.18394.
[46] J.P. Ronaldson, et al., Toward quantifying the composition of soft tissues by spectral CT with Medipix3, Med. Phys. 39 (11) (2012) 6847–6857, https://doi.org/10.1118/1.4760773.
[47] J.M. Boone, J.A. Seibert, An accurate method for computer-generating tungsten anode x-ray spectra from 30 to 140 kV, Med. Phys. 24 (11) (1997) 1661–1670, https://doi.org/10.1118/1.597953.